

Ultrafast atomic-scale scanning tunnelling spectroscopy of a single vacancy in a monolayer crystal

Received: 9 June 2023

Accepted: 9 January 2024

Published online: 14 March 2024

 Check for updatesC. Roelcke^{1,2,4}, L. Z. Kastner^{1,2,4}, M. Graml^{2,3}, A. Biereder^{1,2},
J. Wilhelm^{2,3}✉, J. Repp^{1,2}✉, R. Huber^{1,2}✉ & Y. A. Gerasimenko^{1,2}

Defects in atomically thin semiconductors and their moiré heterostructures have emerged as a unique testbed for quantum science. Strong light–matter coupling, large spin–orbit interaction and enhanced Coulomb correlations facilitate a spin–photon interface for future qubit operations and efficient single-photon quantum emitters. Yet, directly observing the relevant interplay of the electronic structure of a single defect with other microscopic elementary excitations on their intrinsic length, time and energy scales remained a long-held dream. Here we directly resolve in space, time and energy how a spin–orbit-split energy level of an isolated selenium vacancy in a moiré-distorted WSe₂ monolayer evolves under the controlled excitation of lattice vibrations, using lightwave scanning tunnelling microscopy and spectroscopy. By locally launching a phonon oscillation and taking ultrafast energy-resolved snapshots of the vacancy’s states faster than the vibration period, we directly measure the impact of electron–phonon coupling in an isolated single-atom defect. The combination of atomic spatial, sub-picosecond temporal and millielectronvolt energy resolution marks a disruptive development towards a comprehensive understanding of complex quantum materials, where the key microscopic elementary interactions can now be disentangled, one by one.

Atomically thin crystals of transition metal dichalcogenides (TMDCs) and their twisted heterostructures have revolutionized condensed-matter physics. Unusual excitonic properties^{1–3}, valley pseudospin⁴ in combination with strong spin–orbit interaction⁵ and moiré engineering^{2,6,7} have defined a unique toolbox to tailor exotic correlated^{8,9} and topologically non-trivial states¹⁰. TMDC moiré heterostructures have also been proposed as versatile quantum simulators¹¹. Unleashing the full potential of these quantum materials requires a precise in situ understanding of the microscopic dynamics of electrons that underlie such novel functionalities. Recently, time- and angle-resolved

photoelectron spectroscopy has started to provide this insight by directly mapping the energy of electrons as a function of their crystal momentum with simultaneous femtosecond resolution^{6,7,12,13}—arguably the most comprehensive information accessible for delocalized electrons in perfectly periodic crystals.

Yet, a detailed understanding of many exciting phenomena requires local real-space information: the ubiquitous atomic vacancies in TMDC monolayers¹⁴ and moiré heterostructures¹⁵ have sparked enormous interest as versatile single-photon emitters^{16–19} and catalysts for hydrogen extraction²⁰. Additional functionalities are envisioned

¹Institute of Experimental and Applied Physics, University of Regensburg, Regensburg, Germany. ²Regensburg Center for Ultrafast Nanoscopy (RUN), University of Regensburg, Regensburg, Germany. ³Institute of Theoretical Physics, University of Regensburg, Regensburg, Germany. ⁴These authors contributed equally: C. Roelcke, L. Z. Kastner. ✉e-mail: jan.wilhelm@physik.uni-regensburg.de; jascha.repp@physik.uni-regensburg.de; rupert.huber@physik.uni-regensburg.de

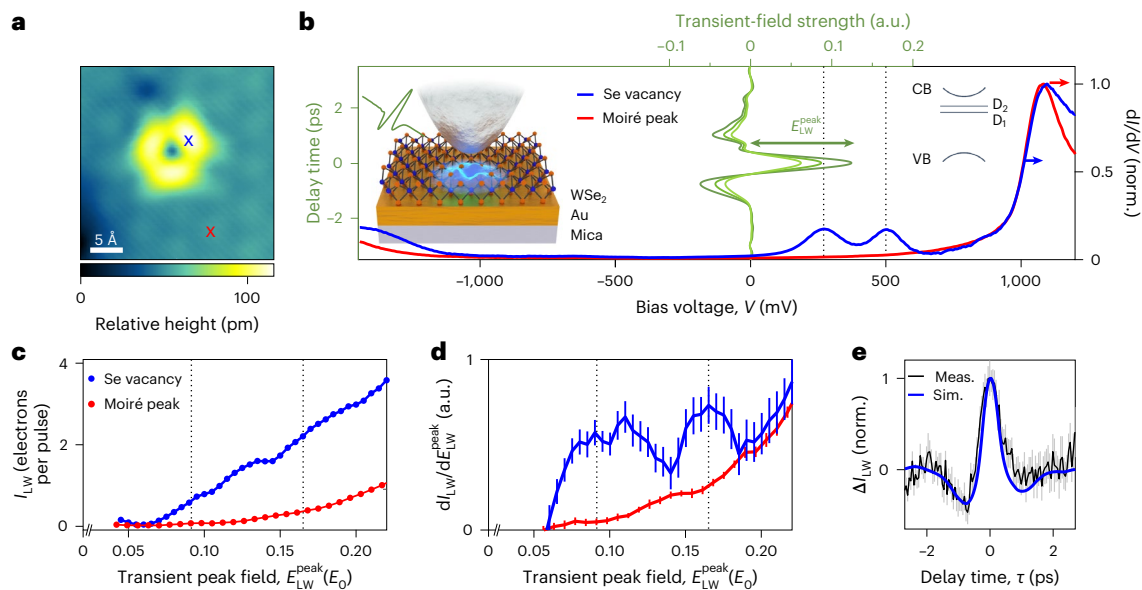


Fig. 1 | Lightwave-driven scanning tunnelling spectroscopy of a single-atom defect in a monolayer of WSe₂. **a**, Constant-current STM image of the Se vacancy in a moiré-distorted (period, ~6 Å) WSe₂ monolayer on Au(111) ($V = 380$ mV, $I = 49$ pA). **b**, Steady-state scanning tunnelling spectrum on the Se vacancy (blue curve) and a moiré peak (red curve) (measurement positions are shown as the crosses in **a**) exhibits two spin-orbit-split²³ defect states at 270 and 500 mV (D_1 and D_2 , respectively; dashed lines) within the bandgap. The left inset (schematic of LW-STS) shows a sub-cycle THz transient focused onto the STM tip and propagating into the near field, where it acts as an ultrafast voltage pulse. By sweeping the field amplitude E_{LW}^{peak} of the far-field transient and hence the peak of the voltage pulse³⁷, that is, $V_{LW}^{\text{peak}} \propto E_{LW}^{\text{peak}}$ (green; Methods discusses the photoassisted sampling^{34,36}), we can sequentially reach the vacancy levels and monolayer conduction band. The right inset shows the schematic of the energy diagram in the (unfolded) WSe₂ Brillouin zone. VB, valence band; CB, conduction band. **c**, Lightwave-driven tunnelling current $I_{LW}(E_{LW}^{\text{peak}})$ recorded on sweeping

the peak electric field on two measurement positions (crosses in **a**), smoothed with a nine-point Savitzky-Golay filter before numerical differentiation to avoid artefacts owing to residual noise between the nearest points (data processing and unattenuated far-field amplitude E_0 ; Methods). **d**, Lightwave-driven scanning tunnelling spectrum $dI_{LW}/dE_{LW}^{\text{peak}}$ showing position-dependent spectral features. **e**, Assessment of an ultrashort tunnelling window by temporal autocorrelation measurement (black) and simulation (blue; the rate equation model is explained in Methods): two pulses with the transient peak field of $0.05E_0$ are overlapped in time, inducing a lightwave-driven tunnelling current dominated by contributions from an ultrashort time window. The data in **d** and **e** are shown as mean values \pm standard deviations of bootstrapped datasets (Methods). In **d**, there are five (two) measurements on Se vacancy (moiré peak) per data point: each measurement containing 219.6 million laser pulses. In **e**, there are 19 measurements per data point (each measurement comprises 15.25 million laser pulses).

through ultrafast light engineering²¹ and site-selective defect generation²². Although steady-state experiments have shed light on distinct energy¹⁴, orbital²³ and spin²⁴ structures of individual defects, an in situ understanding of their dynamical interaction with the environment requires a counterpart of time- and angle-resolved photoelectron spectroscopy, providing ultrafast electronic spectroscopy, yet with direct atomic spatial instead of momentum resolution. Ultrafast near-field microscopy^{25,26} and nanoscale coherent phonon spectroscopy²⁷ have enabled the direct observation of femtosecond charge and lattice dynamics on the nanoscale. In time-integrated studies, strong confinement of light to atomically sharp metallic tips has allowed photoluminescence²⁸ or Raman scattering²⁹ to map molecular levels and vibrational states with ångström (Å) resolution. Lightwave-driven scanning tunnelling microscopy^{30–40} (LW-STM) has combined both atomic spatial and femtosecond temporal resolution^{31,35}, but merging these capabilities with spectroscopic millielectronvolt energy resolution has remained an ambitious vision.

Here we introduce time-resolved lightwave-driven scanning tunnelling spectroscopy (LW-STs) to demonstrate with direct real-space access how atomic motion transiently modulates spin-orbit-split energy levels of a single selenium (Se) vacancy in a moiré-distorted WSe₂ monolayer on gold (Au). Ultrafast snapshots of electronic tunnelling spectra reaching atomic spatial and 300 fs temporal resolution reveal transient energy shifts of the lowest bound defect state by up to 40 meV, depending on the amplitude and phase of the locally excited coherent lattice vibration. In particular, the observed shift is larger than thermal smearing at room temperature. The ability to directly correlate ultrafast electronic energy shifts with local atomic displacement

renders LW-STs a unique tool to decipher the role of local electron-phonon coupling in emerging phases of quantum materials, revealing routes to engineer novel defect-based functionalities using phonons²¹.

Lightwave STS of atomic defect energy levels

The experiments are performed on a monolayer of WSe₂, which was mechanically exfoliated onto an atomically flat Au(111) surface. Rotation and lattice mismatch between WSe₂ and Au cause a hexagonal moiré pattern with a period of ~6 Å (Fig. 1a and Extended Data Fig. 1). A conventional tunnelling spectrum (Fig. 1b) measured at a moiré peak (Fig. 1a, red cross) confirms the semiconducting nature of the monolayer featuring a bandgap with a conduction band edge at 1,100 meV (Fig. 1b, red curve), whereas the small but finite density of states in the gap is related to coupling between the semiconducting monolayer and the metallic substrate⁴¹. The tunnelling spectrum of a single defect (Fig. 1b, blue curve; Fig. 1a, blue cross) exhibits two additional in-gap states with a characteristic three-fold (C_3 -symmetric) orbital structure (Fig. 1a) located at +270 and +500 meV, well separated from the conduction band edge (the band diagram is shown in Fig. 1b, right inset). As reported in other work²³, these features can be identified as spin-orbit-split defect states D_1 and D_2 of an isolated Se vacancy in the top-most Se layer, formed by the dangling bonds of the surrounding atoms.

To directly follow how ultrafast atomic motion transiently influences the energy spectrum of the defect states, we proceed from static to ultrafast tunnelling spectroscopy. The experimental idea expands on the concept of LW-STM^{30–40}, where an ultrashort terahertz (THz) pulse is coupled into the tunnelling junction of the scanning tunnelling microscopy (STM) setup, such that the resulting near-field waveform

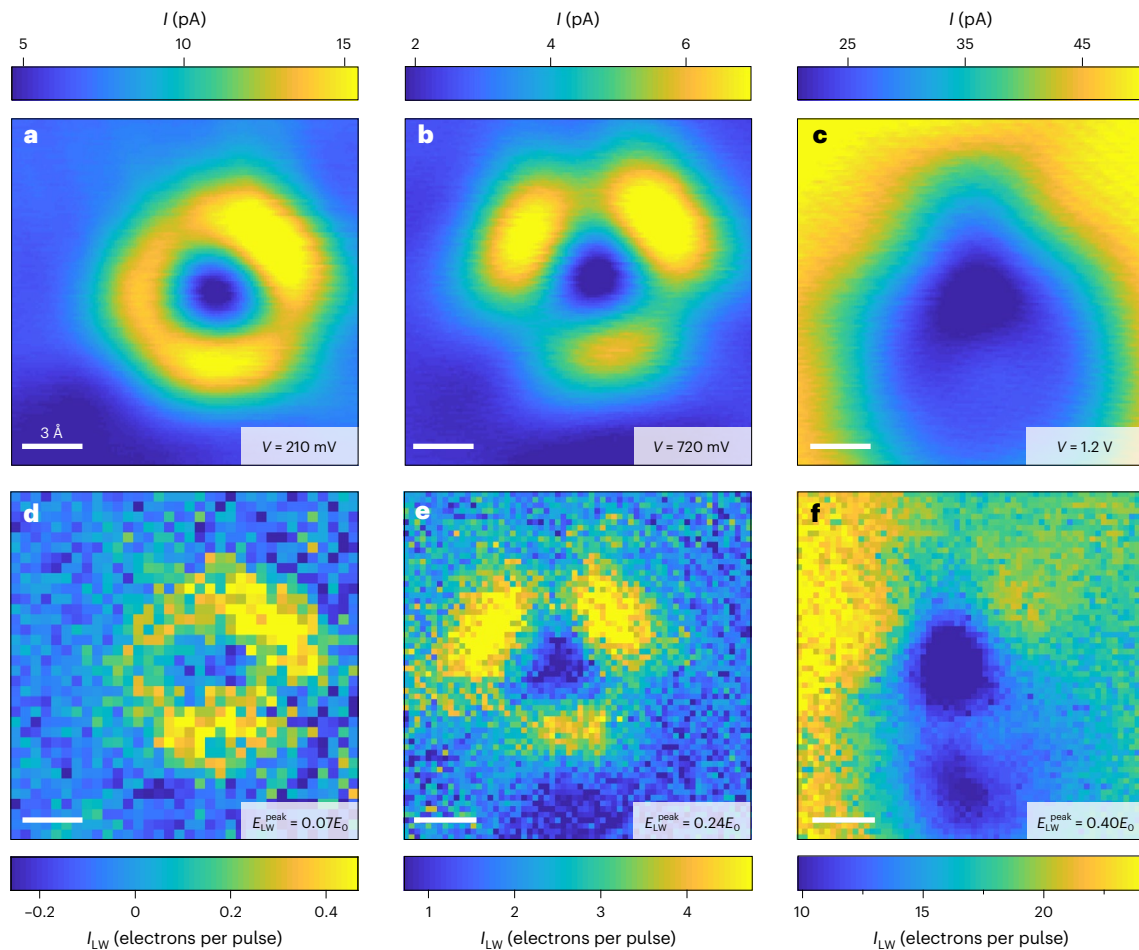


Fig. 2 | Defect-state assignment in ultrafast STM. a–c, Bias-dependent images of the Se vacancy as observed with conventional STM in the constant-height mode (height setpoint, $I = 49$ pA; $V = 700$ mV (a), $V = 1,200$ mV (b,c)). **d–f,** Corresponding images recorded with lightwave-driven STM ($V = 0$) at the equivalent peak fields (height setpoint: $V = 30$ mV, $I = 49$ pA, 1.7 Å approach).

The bias and peak-field values correspond to energies below (a and d) and above (b and e) the defect states, as well as within the conduction band (c and f). In all the panels, the colour bar extends from the third to ninety-seventh percentile of the raw-image current distribution. The LW-STM images are averaged over two (e and f) and ten (d) individual images at the same parameters.

acts as an ultrafast voltage pulse $\mathcal{V}_{\text{LW}}(t)$ (refs. 34,36,37), replacing the static voltage used in conventional STM (Fig. 1b, left inset). In LW-STM, the peak amplitude $V_{\text{LW}}^{\text{peak}}$ of $\mathcal{V}_{\text{LW}}(t)$ is typically kept constant as the tip position is scanned. Conversely, LW-STs can be achieved by systematically scanning the THz peak field $E_{\text{LW}}^{\text{peak}}$ and therefore $V_{\text{LW}}^{\text{peak}}$ (refs. 30–32,37) (Fig. 1b, green traces), while the lightwave-driven current I_{LW} is monitored as a function of $V_{\text{LW}}^{\text{peak}}$. At the same time, atomic spatial resolution³¹ is maintained (Extended Data Fig. 1d). In general, the instantaneous tunnelling current $J_{\text{LW}}(t)$ is generated by a broad range of voltages (Extended Data Fig. 2) up to $V_{\text{LW}}^{\text{peak}}$. The time-integrated net current, namely, $I_{\text{LW}} = \langle J_{\text{LW}}(t) \rangle$, measured in the experiment can, thus, contain tunnelling contributions from multiple states. Even with a known near-field waveform, extracting the lightwave-driven spectrum from such currents usually requires further assumptions^{34,42} (Methods). However, the picture drastically changes for energetically isolated levels or bands, for which state-specific tunnelling can be driven^{31,38}. At the tunnelling onset into a specific state, the instantaneous current can then be strongly confined in time to the field crest of the THz transient³¹ and I_{LW} is dominated by the contribution of J_{LW} at the highest peak $V_{\text{LW}}^{\text{peak}}$ of the voltage transient, such that it approximates the instantaneous tunnelling current. Thus, at least for the rising edge of an effective single-level system, we expect $dI_{\text{LW}}/dV_{\text{LW}}^{\text{peak}}$ to approximate the local density of states (LDOS) measured by $dI/dV(V = V_{\text{LW}}^{\text{peak}})$, as in conventional tunnelling spectroscopy, but on ultrafast timescales (Methods).

We test this idea by positioning the STM tip on the vacancy and the moiré peak and measuring the respective local current I_{LW} (Fig. 1c) as a function of $E_{\text{LW}}^{\text{peak}}$ (quantified in units of the unattenuated THz-field strength E_0 ; Methods). Large currents at the vacancy position along with a vanishing current on the moiré peak signify selective tunnelling into the defect states. Remarkably, the lightwave-driven spectrum $dI_{\text{LW}}/dV_{\text{LW}}^{\text{peak}} \propto dI_{\text{LW}}/dE_{\text{LW}}^{\text{peak}}$ obtained at the defect location (Fig. 1d, blue) exhibits two peaks like those observed in static STS (Fig. 1b), which can be attributed to the two defect states (Extended Data Fig. 2). In contrast, barely any signal is recorded on the moiré peak of the surrounding WSe_2 (Fig. 1d, red) up to the conduction band (Extended Data Fig. 3). Even though the lightwave-driven spectra compare nicely with the steady-state ones, they are not expected to exhibit the same lineshapes, since (1) the tunnelling time window changes with increasing peak electric field and (2) the lightwave may induce dynamics that is probed within the same transient. Owing to the shape of $\mathcal{V}_{\text{LW}}(t)$ and the position of the Fermi level in the bandgap (Fig. 1b), the negative half-cycles of the THz pulse generate no substantial contribution to the net current even at a peak voltage reaching the conduction band minimum. The current induced by the sole positive half-cycle of the transient is almost zero until its peak probes into the lower-energy localized state of the Se vacancy or the conduction band edge in pristine semiconductor regions.

This scenario warrants the lightwave-driven $dI_{\text{LW}}/dV_{\text{LW}}^{\text{peak}}$ spectra to be recorded with ultrafast temporal definition. The achievable

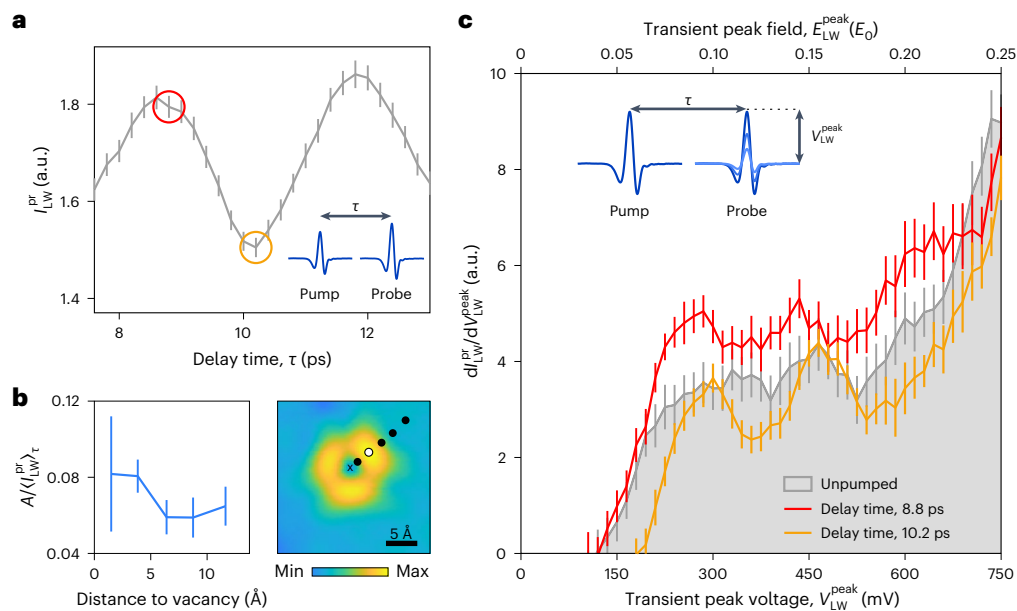


Fig. 3 | Ultrafast modulation of the LDOS of a single defect. a, Tunnelling current driven by the THz probe pulse, $I_{\text{LW}}^{\text{pr}}$, as a function of delay time after a local THz pump pulse excitation (inset) exhibits oscillations on the defect orbital lobe (position highlighted as a white dot in **b** (right)). Pump and probe peak fields are $0.33E_0$ and $0.60E_0$ (that is, 990 mV and 1.80 V), respectively. **b**, Dependence of the amplitude A of oscillations in $I_{\text{LW}}^{\text{pr}}$ normalized by its mean value $\langle I_{\text{LW}}^{\text{pr}} \rangle_{\tau}$ on the STM tip position relative to the vacancy (cross) (right panel) (constant-current STM image: $V = 380$ mV, $I = 49$ pA; colour bar, minimum to maximum apparent height). The peak pump ($0.175E_0$, 525 mV) and probe field ($0.300E_0$, 900 mV) were kept fixed. The data are shown as amplitude of the sinusoidal fit to oscillations in $I_{\text{LW}}^{\text{pr}}$ divided by $\langle I_{\text{LW}}^{\text{pr}} \rangle_{\tau} \pm 95\%$ confidence margin of the amplitude fit. **c**, Ultrafast tunnelling spectra measured at the maximum (8.8 ps; red circle in **a**) and the

minimum (10.2 ps; yellow circle in **a**) of the pump-induced oscillations (pump field: $0.32E_0$, 960 mV) recorded on the orbital lobe (white dot in **b**). On the top/bottom horizontal axis, the unattenuated far-field amplitude E_0 is gauged to a peak voltage $V_{\text{LW}}^{\text{peak}}$ of 3 V. The inset shows the fixed pump-variable probe scheme for the measurement of time-resolved ultrafast tunnelling spectra. Data in **a** and **c** and $I_{\text{LW}}^{\text{pr}}$ used in **b** represent mean values \pm standard deviations of bootstrapped datasets (Methods). Data in **a** include 12 measurements per point, each measurement containing 18.3 million laser pulses. Data in **b** comprise nine measurements of $I_{\text{LW}}^{\text{pr}}$ per delay and position each, and involve 109.8 million laser pulses. Data in **c** include 11 (13 and 10) measurements for 8.8 ps (10.2 ps and unpumped) per delay and peak voltage each, and involve 219.6 million laser pulses per measurement.

temporal resolution is experimentally quantified by autocorrelation measurements (Fig. 1e), where we split the THz pulse into two copies and measure I_{LW} for varying delay times between them. The peak field ($0.05E_0$) is chosen such that only once combined, they open a tunnelling channel into the first defect level (Fig. 1d). Noteworthy, the autocorrelation peak width (Fig. 1e) exhibits a delay-time-dependent change in the tunnelling current ΔI_{LW} on timescales shorter than one picosecond. The measured autocorrelation is reproduced by a rate equation model, which treats the transient occupation of the first defect level, by assuming a 5 fs lifetime of D_1 and utilizing the instantaneous tunnelling rate deduced from the steady-state dI/dV (Methods). This allows us to extract an upper limit for the tunnelling window of about 350 fs in the ± 100 meV vicinity of the first defect level (Extended Data Fig. 2a–c).

Femtosecond STM images taken at different $E_{\text{LW}}^{\text{peak}}$ values can unambiguously connect the fingerprints in the LW-STs spectra with the orbital structure of the corresponding defect states. To this end, we compare the STM images obtained with static (Fig. 2a–c) and THz (Fig. 2d–f) biasing. A nearly circular contrast occurs in both ultrafast (Fig. 2d; $E_{\text{LW}}^{\text{peak}} = 0.07E_0$) and steady-state STM images (Fig. 2a; $V = 210$ mV) below the first tunnelling onset (Fig. 1b,d). For $E_{\text{LW}}^{\text{peak}} > 0.1E_0$, the THz-induced image (Fig. 2e) clearly reproduces the C_3 symmetry of the defect levels (Fig. 2b). Above the conduction band edge (Fig. 2c,f), the defect appears as a depression. Based on the perfect agreement between the steady-state and ultrafast STM images, we assign the first tunnelling onset in $dI_{\text{LW}}/dE_{\text{LW}}^{\text{peak}}$ to the rising edge of the D_1 level of the Se vacancy. The ratio between $E_{\text{LW}}^{\text{peak}}$ and bias V allows us to calibrate the maximum peak THz voltage corresponding to the unattenuated incident field E_0 as $V_{\text{LW}}^{\text{peak}} = (3.0 \pm 0.3)$ V (Extended Data Fig. 2e–g).

Control of single-defect energy by ultrafast atomic motion

Our novel ultrafast spectroscopy of the vacancy's LDOS puts us in a unique position to track the impact of lattice vibrations on single-defect levels in the time domain. To this end, we first establish that a THz pump pulse can excite oscillations in the current driven by a subsequent THz probe pulse, $I_{\text{LW}}^{\text{pr}}$ (Fig. 3a). The oscillation period is ~ 3 ps, with a maximum and a minimum located at a pump–probe delay time of $\tau = 8.8$ ps (red circle) and $\tau = 10.2$ ps (yellow circle), respectively. These oscillations do not occur on a bare Au(111) surface (Extended Data Fig. 4). We repeat the experiment for different tip positions relative to the vacancy (Fig. 3b) and extract the amplitude A of the current oscillations. Since the spatial dependence of the tunnelling current itself (Fig. 2) can affect the current oscillations, we normalize A by the respective delay-time-averaged current, that is, $A/\langle I_{\text{LW}}^{\text{pr}} \rangle_{\tau}$. This relative oscillation amplitude peaks on the vacancy and abruptly drops by $\sim 25\%$ for the pristine surface of the monolayer (Fig. 3b). From these data alone, it is unclear to which extent a potential mechanical motion changing the tip–sample distance or modulations in the energy spectrum contribute to the current oscillations.

Ultrafast tunnelling spectroscopy can disentangle such contributions. To this end, we excite the vacancy at its orbital lobe (Fig. 3b, white dot) with a fixed-strength THz pump pulse and sweep the amplitude of the time-delayed probe pulse (Fig. 3c, inset) to retrieve the transient spectra (Fig. 3c). The numerical derivative, $dI_{\text{LW}}^{\text{pr}}/dV_{\text{LW}}^{\text{peak}} (V_{\text{LW}}^{\text{peak}})_{\tau}$, extracted from these experimental data, thus, reflects the energy- and delay-time-resolved LDOS. An overall vertical rescaling of the entire spectra indicates a change in the tunnel overlap of the tip and sample wavefunctions. We assign the change in overlap to a mechanical out-of-plane motion of the whole layer because the oscillations of $I_{\text{LW}}^{\text{pr}}$

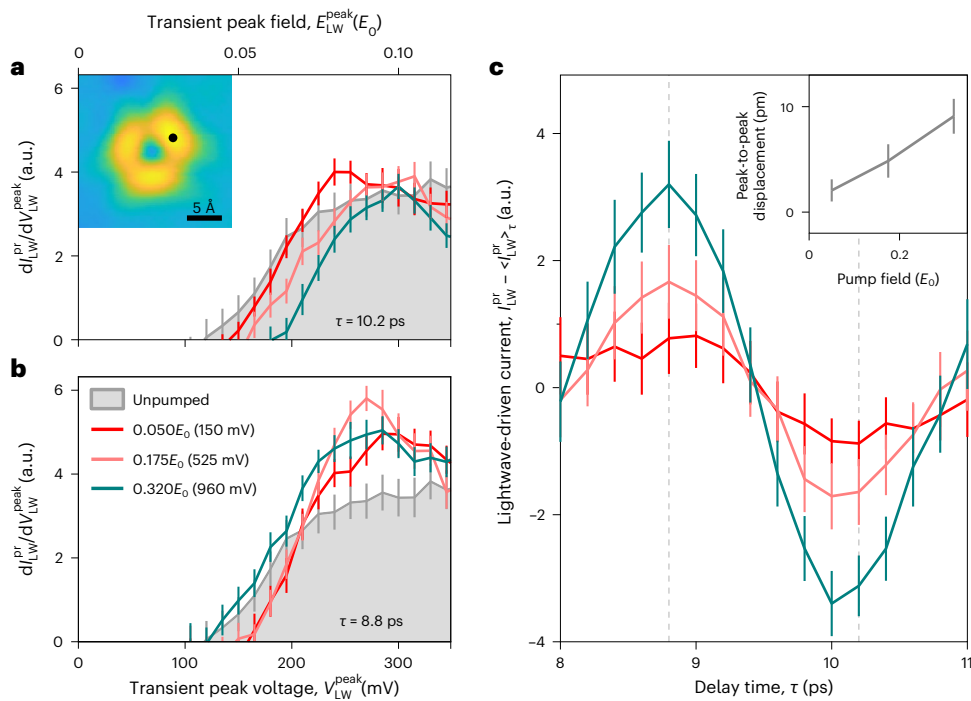


Fig. 4 | Pump-field-dependent transient level shift and ultrafast dynamics. **a,b**, Ultrafast tunnelling spectra of the Se vacancy (measurement position shown in the inset) measured at delay times of $\tau = 10.2$ ps (**a**) and $\tau = 8.8$ ps (**b**) with different THz pump-field strengths (the legend shown in **b** applies to the data in all panels). The data for 10.2 ps reveal a distinct monotonic field-dependent shift in the tunnelling onset into the first defect level, whereas for $\tau = 8.8$ ps, the energy shift occurs for low pump fields only ($0.050E_0$ and $0.175E_0$). **c**, Oscillations in probe current $I_{\text{LW}}^{\text{pr}} - \langle I_{\text{LW}}^{\text{pr}} \rangle_{\tau}$ for the three pump fields as a function of delay time (probe field, $0.32E_0$, 960 mV). The inset shows the structural peak-to-peak

displacement as a function of the pump field, extracted from the oscillations in probe current using the exponential dependence of $I_{\text{LW}}^{\text{pr}}$ on the tip-sample distance (Extended Data Fig. 6). Data in **a–c** represent mean values \pm standard deviations of the bootstrapped datasets (Methods). Three (five) (data in **a**) and five (five) (data in **b**) measurements per data point for pump fields of $0.175E_0$ ($0.050E_0$); for $0.320E_0$, see Fig. 3c. Each measurement involves 219.6 million laser pulses. In **c**, $I_{\text{LW}}^{\text{pr}}$ comprises 18 (54) measurements for $0.175E_0$ and $0.320E_0$ ($0.050E_0$) per delay each; 36.6 million laser pulses are used per measurement.

are not limited to the vacancy position (Fig. 3b). Importantly, beyond this overall rescaling, the transient LDOS of the vacancy exhibits variations with τ in its lineshape. Specifically, the rising edge of D_1 , at $E_{\text{LW}}^{\text{peak}} \approx 0.05E_0$, shifts horizontally with τ ; the onset aligns with the unpumped spectrum (Fig. 3c, grey curve) for $\tau = 8.8$ ps (red curve), but moves towards a larger voltage, for $\tau = 10.2$ ps (yellow curve). The dynamics of the rising edge of D_1 may be affected by changes in the width and position of D_1 . However, the comparable shape of the pumped spectra around D_1 suggests that the shift in the tunnelling onset is dominated by a transient shift in the defect level in energy. The observed shift by $-0.014E_0$ (Methods) corresponds to an energy modulation of -40 meV following from our previous calibration.

To scrutinize the origin of shifts in the ultrafast tunnelling spectra, we compare the results for different pump pulse strengths (Fig. 4). At $\tau = 10.2$ ps (Fig. 4a), the D_1 rising edge shifts to higher energies with increasing pump amplitudes in a monotonic and roughly linear fashion (Extended Data Fig. 5). Meanwhile, at $\tau = 8.8$ ps (Fig. 4b), moderate pump fields ($0.050E_0$ and $0.175E_0$) promote this rising edge to higher energies, whereas at the highest pump field of $0.320E_0$, the onset shifts back resembling the unpumped one. Such non-monotonic behaviour strongly suggests the presence of competing mechanisms responsible for the shift in the tunnelling onset into D_1 .

We estimate the magnitude of the mechanical out-of-plane motion from current oscillations at large probe fields (Fig. 3a), where the contribution from shifts in the tunnelling onset in the defect level to the current $I_{\text{LW}}^{\text{pr}}$ becomes negligible and cannot account for the $\sim 10\%$ pump-induced variation in $I_{\text{LW}}^{\text{pr}}$. Therefore, we attribute the oscillations of the current at large $V_{\text{LW}}^{\text{peak}}$ to predominantly originate from a modulation of the tip-sample distance, as also supported by the qualitative similarities of oscillations on and off defects (Extended Data Fig. 4c,d).

When $V_{\text{LW}}^{\text{peak}}$ reaches the conduction band edge ($0.320E_0$), the amplitude of the probe-current oscillation, $I_{\text{LW}}^{\text{pr}} - \langle I_{\text{LW}}^{\text{pr}} \rangle_{\tau}$, as a function of delay time (Fig. 4c) linearly depends on the pump-field strength, whereas the frequency remains constant within the error bars. The measured current oscillation corresponds to an out-of-plane motion with an ~ 10 pm peak-to-peak displacement at the maximum pump field (Fig. 4c, inset, and Extended Data Fig. 6). This is slightly larger than the few-picometre relative height of the moiré pattern (Extended Data Fig. 1c).

Understanding the origin of the time-dependent D_1 -level shift requires us to first explore the nature of the pump-induced atomic displacements. The oscillations are unambiguously associated with the WSe_2 monolayer as they vanish on pristine Au (Extended Data Fig. 4a). The low frequency of vibrations suggests an acoustic character of the corresponding phonon. Moreover, the out-of-plane oscillations are observable over a 100 ps range (Extended Data Fig. 7), evidencing a specific standing-wave mode rather than a travelling wave packet. To elucidate the emergent phonon modes in the WSe_2/Au heterostructures, we performed first-principles calculations (Methods), which reveal (Fig. 5a) that one of the degenerate out-of-plane transverse acoustic modes becomes gapped at the Γ point, whereas the other mode (ZA) starts from zero energy and momentum. The gapped mode (Fig. 5a, DM; red curve) corresponds to a drum-like vertical motion of WSe_2 relative to the Au layers. At the Γ point, the monolayer predominantly moves as a whole, accompanied by smaller intralayer distortions (Fig. 5b). It is plausible that the atomically strong, predominantly out-of-plane THz electric near field efficiently couples to this drum mode (DM) by Coulomb interaction with charges in the heterostructure (for example, charge transfer between Au and WSe_2) and by its field-induced polarization⁴⁰. The linear dependence of the oscillation amplitude on the applied electric field (Fig. 4c, inset) suggests that the former

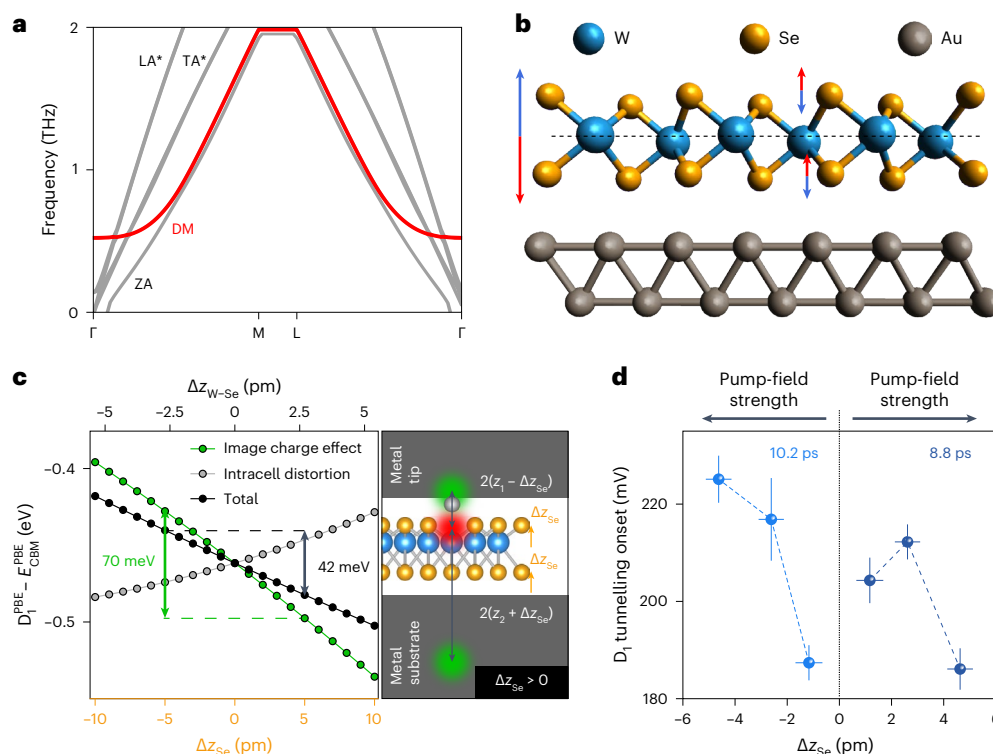


Fig. 5 | Drum mode of monolayer WSe₂ on Au(111) and its impact on the D₁ level. **a**, First-principles calculation of the low-energy part of the phonon spectrum, showing the longitudinal (LA*) and transverse (TA* and ZA) acoustic branches alongside the DM that splits off the ZA branch and is gapped (−0.5 THz) at the Γ point of the unfolded Brillouin zone of the WSe₂ monolayer (Methods provides the calculation details). **b**, Real-space visualization of the atomic displacements (red and blue arrows) in the uniform monolayer caused by DM at the Γ point. The displacements are shown as the centre-of-mass motion of the WSe₂ monolayer (dashed line) and intralayer atomic shifts. The Au atoms are kept fixed. **c**, First-order effects of DM-induced atomic displacements on the defect-level energy: image charge effect (green) and cell geometric distortion (grey) (Methods provides the simulation details). The D₁^{PBE} energy level is shown relative to the conduction band minimum. Here Δz_{Se} denotes the vertical displacement of Se atoms and $\Delta z_{\text{W-Se}}$ is the relative, intracell displacement

between the W and Se atoms. A positive Δz_{Se} corresponds to the monolayer being closer to the tip. Schematic of the simulation geometry (right), visualized like that in Extended Data Fig. 9. The atomic displacements are exaggerated by a factor of 100 for illustration purposes. The red dot indicates the defect and the green dots are the image charges in the tip and substrate. Also, z_1 (z_2) denotes the equilibrium distance between the defect and tip (substrate) image plane. **d**, Experimental D₁ onsets (Methods provides the means for quantifying onsets) projected onto the estimated displacements. The mean and error bars of the latter are extracted from the mean values \pm standard deviation of the respective $I_{\text{LW}}^{\text{pr}}$ of the bootstrapped currents (Methods), using the dependence of $I_{\text{LW}}^{\text{pr}}(\Delta z)$ (Extended Data Fig. 6). The same datasets as those in Fig. 4a,b, evaluated at a probe field of $0.28E_0$. The vertical error bars correspond to the ones shown in Extended Data Fig. 5c.

mechanism dominates. Less prevalent in- and out-of-plane vibrational components may also occur but will quickly decohere because of their dispersing frequencies.

Finally, we discuss how the atomic displacements may shift the D₁ energy. Most directly, the centre-of-mass motion of the WSe₂ monolayer modulates the Coulomb interaction of the D₁ level with its image charge distribution⁴³ in the Au substrate and/or the tip. In addition, the intracell motion of W and Se atoms within the DM (Fig. 5b) can slightly change the orbital hybridizations. Image charge contributions can be analytically included to the leading order (Methods). To estimate the effect of intracell motion, we introduce atomic displacements induced by the DM in a uniform monolayer (Fig. 5b), remove one Se atom and calculate the ab initio electronic spectrum of such a monolayer in the absence of Au (Methods). Figure 5c shows that both effects scale linearly in good approximation with the displacement and compete with each other, the image charge effect being the larger one. Remarkably, this simplified approach provides an estimate in the right order of magnitude for the level shifts.

Linear effects dominate for larger displacements (Fig. 5d). Simultaneously, there appear to be smaller higher-order corrections on top. These enhance the linear shift for negative displacements (monolayer closer to Au) and partially counteract the shift for positive excursions, resulting in an overall non-monotonic asymmetric

shift. However, the nonlinear effect seen in the experiment is not fully reproduced by theory, which has to rely on model assumptions since a full time-dependent atomistic treatment covering the different length scales of the experiment is currently out of reach computationally. We hope that our study triggers future theory developments improving the above approach, for example, by changing screening due to phonon motion beyond the image charge effect. Kinetic and chemical stabilities of the atomic structure in the vicinity of the vacancy further challenge the calculations.

Discussion and conclusions

The combination of atomic³¹, sub-picosecond and 10-meV-scale resolution in LW-STs allowed us to observe how the energy levels of a single Se vacancy evolve during dynamic atomic displacements. We revealed how the excitation of an acoustic DM adiabatically shifts the first defect level on timescales shorter than the oscillation period. The unexpected unipolar and non-monotonic behaviour of the shift with the oscillation amplitude stems from a complex interplay of lattice distortions. Our results, thus, establish ultrafast spectroscopy on atomic length scales, the sought-after single-entity and real-space access of which complements techniques operating in momentum space, such as time-resolved photoemission orbital tomography⁴⁴. Simultaneous access to atomic vibrations on their intrinsic length scales and timescales provides all

the necessary tools to decipher local electron–phonon coupling—including nonlinearities and coherences, which have proved challenging before^{45,46}. Combined with the pulse shaping of a pump pulse, our technique opens new pathways to excite specific atomically localized vibrations and consequently locally control many-body electronic states by transiently shifting their energetic position by a desired value. With the ability to directly access the ultrafast LDOS, we envision the direct real-space observation of moiré exciton trapping⁴⁷ as well as the transient driving of phase transitions into high-temperature superconductivity and other exotic states of matter.

Online content

Any methods, additional references, Nature Portfolio reporting summaries, source data, extended data, supplementary information, acknowledgements, peer review information; details of author contributions and competing interests; and statements of data and code availability are available at <https://doi.org/10.1038/s41566-024-01390-6>.

References

1. Wang, G. et al. Colloquium: excitons in atomically thin transition metal dichalcogenides. *Rev. Mod. Phys.* **90**, 021001 (2018).
2. Ciarrocchi, A., Tagarelli, F., Avsar, A. & Kis, A. Excitonic devices with van der Waals heterostructures: valleytronics meets twistrionics. *Nat. Rev. Mater.* **7**, 449–464 (2022).
3. Naik, M. H. et al. Intralayer charge-transfer moiré excitons in van der Waals superlattices. *Nature* **609**, 52–57 (2022).
4. Xu, X., Yao, W., Xiao, D. & Heinz, T. F. Spin and pseudospins in layered transition metal dichalcogenides. *Nat. Phys.* **10**, 343–350 (2014).
5. Manchon, A., Koo, H. C., Nitta, J., Frolov, S. M. & Duine, R. A. New perspectives for Rashba spin-orbit coupling. *Nat. Mater.* **14**, 871–882 (2015).
6. Karni, O. et al. Structure of the moiré exciton captured by imaging its electron and hole. *Nature* **603**, 247–252 (2022).
7. Schmitt, D. et al. Formation of moiré interlayer excitons in space and time. *Nature* **608**, 499–503 (2022).
8. Xu, Y. et al. Correlated insulating states at fractional fillings of moiré superlattices. *Nature* **587**, 214–218 (2020).
9. Zhou, Y. et al. Bilayer Wigner crystals in a transition metal dichalcogenide heterostructure. *Nature* **595**, 48–52 (2021).
10. Mak, K. F. & Shan, J. Semiconductor moiré materials. *Nat. Nanotechnol.* **17**, 686–695 (2022).
11. Kennes, D. M. et al. Moiré heterostructures as a condensed-matter quantum simulator. *Nat. Phys.* **17**, 155–163 (2021).
12. Madéo, J. et al. Directly visualizing the momentum-forbidden dark excitons and their dynamics in atomically thin semiconductors. *Science* **370**, 1199–1204 (2020).
13. Ito, S. et al. Build-up and dephasing of Floquet–Bloch bands on subcycle timescales. *Nature* **616**, 696–701 (2023).
14. Hong, J. et al. Exploring atomic defects in molybdenum disulfide monolayers. *Nat. Commun.* **6**, 6293 (2015).
15. Guo, H., Zhang, X. & Lu, G. Moiré excitons in defective van der Waals heterostructures. *Proc. Natl Acad. Sci. USA* **118**, e2105468118 (2021).
16. He, Y.-M. et al. Single quantum emitters in monolayer semiconductors. *Nat. Nanotechnol.* **10**, 497–502 (2015).
17. Srivastava, A. et al. Optically active quantum dots in monolayer WSe₂. *Nat. Nanotechnol.* **10**, 491–496 (2015).
18. Tonndorf, P. et al. Single-photon emission from localized excitons in an atomically thin semiconductor. *Optica* **2**, 347–352 (2015).
19. Chakraborty, C., Kinnischtzke, L., Goodfellow, K. M., Beams, R. & Vamivakas, A. N. Voltage-controlled quantum light from an atomically thin semiconductor. *Nat. Nanotechnol.* **10**, 507–511 (2015).
20. Li, H. et al. Activating and optimizing MoS₂ basal planes for hydrogen evolution through the formation of strained sulphur vacancies. *Nat. Mater.* **15**, 48–53 (2016).
21. Disa, A. S., Nova, T. F. & Cavalleri, A. Engineering crystal structures with light. *Nat. Phys.* **17**, 1087–1092 (2021).
22. Klein, J. et al. Site-selectively generated photon emitters in monolayer MoS₂ via local helium ion irradiation. *Nat. Commun.* **10**, 2755 (2019).
23. Schuler, B. et al. Large spin-orbit splitting of deep in-gap defect states of engineered sulfur vacancies in monolayer WS₂. *Phys. Rev. Lett.* **123**, 076801 (2019).
24. Cochrane, K. A. et al. Spin-dependent vibronic response of a carbon radical ion in two-dimensional WS₂. *Nat. Commun.* **12**, 7287 (2021).
25. Sternbach, J. et al. Programmable hyperbolic polaritons in van der Waals semiconductors. *Science* **371**, 617–620 (2021).
26. Plankl, M. et al. Subcycle contact-free nanoscopy of ultrafast interlayer transport in atomically thin heterostructures. *Nat. Photon.* **15**, 594–600 (2021).
27. Liu, S. et al. Nanoscale coherent phonon spectroscopy. *Sci. Adv.* **8**, eabq5682 (2022).
28. Yang, B. et al. Sub-nanometre resolution in single-molecule photoluminescence imaging. *Nat. Photon.* **14**, 693–699 (2020).
29. Lee, J., Crampton, K. T., Tallarida, N. & Apkarian, V. A. Visualizing vibrational normal modes of a single molecule with atomically confined light. *Nature* **568**, 78–82 (2019).
30. Cocker, T. L. et al. An ultrafast terahertz scanning tunnelling microscope. *Nat. Photon.* **7**, 620–625 (2013).
31. Cocker, T. L., Peller, D., Yu, P., Repp, J. & Huber, R. Tracking the ultrafast motion of a single molecule by femtosecond orbital imaging. *Nature* **539**, 263–267 (2016).
32. Yoshioka, K. et al. Real-space coherent manipulation of electrons in a single tunnel junction by single-cycle terahertz electric fields. *Nat. Photon.* **10**, 762–765 (2016).
33. Jelic, V. et al. Ultrafast terahertz control of extreme tunnel currents through single atoms on a silicon surface. *Nat. Phys.* **13**, 591–598 (2017).
34. Yoshida, S. et al. Subcycle transient scanning tunneling spectroscopy with visualization of enhanced terahertz near field. *ACS Photonics* **6**, 1356–1364 (2019).
35. Peller, D. et al. Sub-cycle atomic-scale forces coherently control a single-molecule switch. *Nature* **585**, 58–62 (2020).
36. Müller, M., Martín Sabanés, N., Kampfrath, T. & Wolf, M. Phase-resolved detection of ultrabroadband THz pulses inside a scanning tunneling microscope junction. *ACS Photonics* **7**, 2046–2055 (2020).
37. Peller, D. et al. Quantitative sampling of atomic-scale electromagnetic waveforms. *Nat. Photon.* **15**, 143–147 (2021).
38. Ammerman, S. E. et al. Lightwave-driven scanning tunnelling spectroscopy of atomically precise graphene nanoribbons. *Nat. Commun.* **12**, 6794 (2021).
39. Wang, L., Xia, Y. & Ho, W. Atomic-scale quantum sensing based on the ultrafast coherence of an H₂ molecule in an STM cavity. *Science* **376**, 401–405 (2022).
40. Sheng, S. et al. Launching coherent acoustic phonon wave packets with local femtosecond Coulomb forces. *Phys. Rev. Lett.* **129**, 043001 (2022).
41. Sørensen, G., Füchtbauer, H. G., Tuxen, A. K., Walton, A. S. & Lauritsen, J. V. Structure and electronic properties of in situ synthesized single-layer MoS₂ on a gold surface. *ACS Nano* **8**, 6788–6796 (2014).

42. Ammerman, S. E., Wei, Y., Everett, N., Jelic, V. & Cocker, T. L. Algorithm for subcycle terahertz scanning tunneling spectroscopy. *Phys. Rev. B* **105**, 115427 (2022).
43. Neaton, J. B., Hybertsen, M. S. & Louie, S. G. Renormalization of molecular electronic levels at metal-molecule interfaces. *Phys. Rev. Lett.* **97**, 216405 (2006).
44. Wallauer et al. Tracing orbital images on ultrafast time scales. *Science* **371**, 1056–1059 (2021).
45. Gerber, S. et al. Femtosecond electron-phonon lock-in by photoemission and X-ray free-electron laser. *Science* **357**, 71–75 (2017).
46. Na, M. X. et al. Direct determination of mode-projected electron-phonon coupling in the time domain. *Science* **366**, 1231–1236 (2019).
47. Refaely-Abramson, S., Qiu, D. Y., Louie, S. G. & Neaton, J. B. Defect-induced modification of low-lying excitons and valley selectivity in monolayer transition metal dichalcogenides. *Phys. Rev. Lett.* **121**, 167402 (2018).

Publisher's note Springer Nature remains neutral with regard to jurisdictional claims in published maps and institutional affiliations.

Open Access This article is licensed under a Creative Commons Attribution 4.0 International License, which permits use, sharing, adaptation, distribution and reproduction in any medium or format, as long as you give appropriate credit to the original author(s) and the source, provide a link to the Creative Commons licence, and indicate if changes were made. The images or other third party material in this article are included in the article's Creative Commons licence, unless indicated otherwise in a credit line to the material. If material is not included in the article's Creative Commons licence and your intended use is not permitted by statutory regulation or exceeds the permitted use, you will need to obtain permission directly from the copyright holder. To view a copy of this licence, visit <http://creativecommons.org/licenses/by/4.0/>.

© The Author(s) 2024

Methods

STM setup

The home-built STM was operated in ultrahigh vacuum (pressure, $\sim 8 \times 10^{-11}$ mbar) and cryogenic (6.5 K) conditions. The bias voltage was applied to the sample. A home-built high-gain (2.5×10^{10} V A $^{-1}$) transimpedance preamplifier was mounted close to the STM head. The collimated THz beam entered the vacuum chamber through a sapphire window and was focused onto the tunnelling junction by a parabolic mirror mounted on the STM stage. The high stability of our setup allowed us to perform experiments under the same conditions, spanning a time window of about 45 h limited only by the cryogenic setup.

THz generation and characterization

In lithium niobate, phase-locked THz pulses (centre frequency, 1 THz) were generated by tilted-pulse-front optical rectification of 250 fs near-infrared pulses centred at 1,028 nm from a commercial 10 W regenerative laser amplifier operating at a repetition rate of 610 kHz (Light Conversion PHAROS). The THz pulses were split into pairs of mutually delayed THz transients, referred to as pump and probe, using a Michelson interferometer setup. The delay time was controlled with a motorized linear translation stage in one of the arms. The electric field of the THz transients was independently attenuated using a pair of wire-grid polarizers (wire spacing, 30 μ m; wire diameter, 10 μ m) in each arm, rescaling the THz waveform and leaving its shape intact. The whole optical setup was operated in a nitrogen atmosphere.

Far-field THz waveforms were measured outside the ultrahigh-vacuum chamber using electro-optic sampling in ZnTe. The unattenuated electric far field yields a peak amplitude of $E_0 = 0.4$ kV cm $^{-1}$. The near-field waveforms used for the simulations (Extended Data Fig. 2) were independently measured in situ using the photon-assisted emission scheme^{34,36}. The emission was driven by ultrashort near-infrared pulses focused onto the tip apex. The near-infrared pulses for both electro-optic sampling and photoemission measurements were produced by supercontinuum generation in a 5 mm sapphire crystal and subsequently compressed in a prism compressor.

Sample preparation

A freshly cleaved WSe₂ single crystal (hq graphene) was pressed onto a sputtered and flash-annealed (herringbone) atomically flat Au(111) surface in a nitrogen environment. This resulted in large-area monolayer exfoliation owing to the strong adhesion of WSe₂ to Au (ref. 48). Before transfer into the cryogenic STM chamber, the whole structure was then annealed at 360 °C in an ultrahigh vacuum for several hours to ensure the creation of unoxidized Se vacancies, until the pressure stayed on the order of 10^{-9} mbar. The TMDC monolayer is known to hybridize with Au (ref. 49) and its band structure is sensitive to local inhomogeneities in Au under the monolayer⁵⁰. Therefore, we selected defects in areas of an otherwise uniform TMDC on Au(111).

Height setpoint for LW-STs/LW-STM

The STM used in this work allows for extended open-loop operation with negligible changes in the tip position. Unless noted otherwise, each measurement started with stabilizing the tip-sample separation on a defect-free spot on the monolayer, at $V = 30$ mV and $I = 50$ pA in the d.c. regime with THz radiation blocked. With the feedback loop open, V was set to zero and the tip was approached by another $\Delta z = -1.7$ Å. In the measurement shown in Fig. 3a, the same procedure with the parameter set of $V = 100$ mV, $I = 5$ pA and $\Delta z = -3.2$ Å was used instead, resulting in approximately the same tip height. At such tip-sample separations, we reach a sufficient signal-to noise ratio and remain in the regime of tunnelling currents below one electron per pulse when probing the D₁ onset. As the tip is brought closer compared with the steady-state mode, the spatial resolution is expected to be at least as good³⁸.

Detection scheme

To obtain the ultrafast tunnelling spectra, $dI_{\text{LW}}/dV_{\text{LW}}^{\text{peak}}$, in the presence of the pump pulse, we used the following detection scheme. We modulated both pulses at a frequency of $f_1 = 713$ Hz with an optical chopper to extract the total THz-driven signal by lock-in detection. We then additionally modulated the probe pulse at a frequency of $f_2 = 31$ Hz with a second chopper, allowing us to use a lock-in amplifier to demodulate the fraction of the total THz-driven signal that originates from the probe pulse when the pump pulse is present. In effect, this results in a sideband detection at the difference frequency of $f_1 - f_2$.

Differentiation of spectra

To extract the ultrafast tunnelling spectra, $I_{\text{LW}}(E_{\text{LW}}^{\text{peak}})$ was smoothed (Fig. 1c) and then differentiated (Fig. 1d). The robustness of this approach was checked on many Se vacancies. Extended Data Fig. 8a,b shows an example dataset and the corresponding derivative, respectively. All time-resolved measurements were taken under exactly the same experimental conditions in one measurement cycle, ensuring their comparability. Some datasets were polluted by artefacts from reflections off beam blocks or wire-grid polarizers in the setup. For the data shown in Fig. 1c, non-smoothed data with subtracted artefactual current offset (minimum current value, measured at low fields) are shown in Extended Data Fig. 8c. The attenuating polarizer for the probe field caused a reflection that induced a measurable current at low peak fields, quickly vanishing for higher peak voltages. This resulted in an artefactual negative differential conductance in the lightwave-driven spectra for peak fields below $0.05E_0$. We emphasize that the reflected field does not depend on the pump-probe delay time and hence does not affect the conclusions made. In additional measurements, we ensured that no artefactual sources affect the tunnelling onset into the first defect level (Extended Data Fig. 8d).

Error estimation using bootstrap

The error bars for I_{LW} and $dI_{\text{LW}}/dE_{\text{LW}}^{\text{peak}}$ shown throughout the paper were estimated using the standard bootstrap method⁵¹. To this end, mean values of I_{LW} obtained for given external parameters (delay time and pump and probe fields) in N different measurement cycles were randomly resampled with replacement $M \times N$ times (that is, each element can be selected more than once), such that the result contained M sequences of N elements ($M = 10,000$; N defined in the corresponding figure captions). Next, the mean value $\langle I_{\text{LW}} \rangle_m$, where $m \in \{M\}$, was calculated for each sequence. The error bar of I_{LW} was then obtained as the standard deviation of $\langle I_{\text{LW}} \rangle_m$. The error bar of the derivative was similarly retrieved as the standard deviation of $d\langle I_{\text{LW}} \rangle_m/dE_{\text{LW}}^{\text{peak}}$. The two transient spectra shown in Fig. 3c were obtained by averaging $n = 11$ (13) measurements performed on the same defect for 8.8 ps (10.2 ps). The bootstrap error bar is the statistical measure of how much the specific choice—there are $\tilde{C}_n^n = \frac{(2n-1)!}{n!(n-1)!}$ combinations with repetitions—of curves for averaging affects the mean value. The distribution of mean values in bootstrap is approximated by the normal distribution⁵¹.

Autocorrelation simulation

To fit the autocorrelation data in Fig. 1e, two contributions were considered. First, tunnelling through the first defect level was modelled using the rate equation

$$\frac{dN}{dt} = -\frac{N}{\tau_{\text{LT}}} + \alpha(t, \tau) \times (1 - N),$$

where N is the occupation of the first defect level, t is time and τ is the autocorrelation delay time between the two waveforms that were overlapped. The peak voltage of both transients was tuned to 150 mV in the simulation. Interpreted as lifetime broadening, the peak width of the Lorentzian-shaped peak in the steady-state dI/dV spectrum corresponds to a lifetime of a charge in the first defect level of $\tau_{\text{LT}} = 5$ fs.

As this is short compared with the relevant timescales of THz probing, the precise value of τ_{LT} does not affect the simulation. $\alpha(v_{\text{LW}}(t, \tau))$ denotes the instantaneous tunnelling rate from the tip into the first defect level. It was derived under the assumption that the instantaneous tunnelling rate is equal to the steady-state tunnelling rate under the same bias conditions. The scaling of α as a function of the total instantaneous voltage $v_{\text{LW}}(t, \tau)$ was extracted from the steady-state dI/dV spectrum by integration over V . In the autocorrelation experiment, the current was kept slightly below one electron per pulse pair. In this regime, at the given lifetimes, artefacts from Coulomb blockade effects can be excluded. The rate equation was numerically solved for each autocorrelation delay time τ to extract the instantaneous tunnelling current $J_{\text{LW}}^{\text{defect}}(t, \tau)$.

Second, subtracting the defect-level Lorentzians from the steady-state dI/dV curve, a background spectrum was extracted and fitted by a polynomial. Its contribution $J_{\text{LW}}^{\text{bg}}(t, \tau)$ to the overall tunnelling current was calculated as the integral over the polynomial fit from 0 V to the instantaneous voltage $v_{\text{LW}}(t, \tau)$. For this contribution to the tunnelling current, a vanishing lifetime was assumed. For each delay time τ between the two THz pulses, we integrated the sum of $J_{\text{LW}}^{\text{defect}}(t, \tau)$ and $J_{\text{LW}}^{\text{bg}}(t, \tau)$ over t to extract the total autocorrelation tunnelling current, which was then compared with the experimental autocorrelation curve.

Interpretation of lightwave-driven tunnelling spectra

Lightwave-driven tunnelling spectra $dI_{\text{LW}}/dV_{\text{LW}}^{\text{peak}}$ can approximate the steady-state LDOS ($\propto dI/dV$) in the single-electron regime, for example, for a rectangular-shaped transient. In this case, the spectrum yields

$$\frac{dI_{\text{LW}}^{\text{peak}}}{dV_{\text{LW}}^{\text{peak}}} \propto \frac{d}{dV_{\text{LW}}^{\text{peak}}} \int_{-\infty}^{+\infty} J_{\text{LW}}(v_{\text{LW}}(t)) dt \approx \frac{d}{dV_{\text{LW}}^{\text{peak}}} \int_{-\infty}^{+\infty} J_{\text{LW}}(V_{\text{LW}}^{\text{peak}}) \times \Theta(t - t_{\text{peak}} + t_0) \times \Theta(-t + t_{\text{peak}} + t_0) dt \propto \frac{dJ_{\text{LW}}(V_{\text{LW}}^{\text{peak}})}{d(V_{\text{LW}}^{\text{peak}})},$$

where $\Theta(t)$ is the Heaviside function and $2t_0$ is the tunnelling window. For a realistic lightwave transient, as the peak electric field is ramped up, the tunnelling time window for low-lying states becomes wider, such that t_0 in the above equation would become a function of $V_{\text{LW}}^{\text{peak}}$. This is one of the reasons why the approximation works best where the LDOS is sharply defined, such that the density of states effectively gates the voltage pulse. For broad levels, this is true for the tunnelling onset only.

Hence, the low-lying states contribute to the lightwave-driven current at $V_{\text{LW}}^{\text{peak}}$ far above their respective energies. In our measurements, the lightwave-driven current at $V_{\text{LW}}^{\text{peak}} > D_1, D_2$ increases owing to the contribution of the defect states. A pump-induced shift in D_1 can also affect the measured lightwave-driven current. For a 40 meV shift, a simplistic instantaneous tunnelling simulation yields a change of 1.5% in the rectified current at a peak bias of 1.4 V.

Similar to the tunnelling onset into D_1 , at peak fields reaching D_2 , an increasing tunnelling current is associated with the onset of tunnelling into the D_2 level (Extended Data Fig. 2d), which results in a peak-like feature in $dI_{\text{LW}}/dE_{\text{peak}}$ (Extended Data Fig. 2g,h). However, owing to the close proximity of D_1 and D_2 , D_1 can still impact the averaged tunnelling current at a peak field tuned to D_2 . To refrain from interpreting the mixture of multiple energy states, we concentrated on studying state-selective tunnelling onsets only—into D_1 or the conduction band minimum—where a fully data-driven approach can be used.

To avoid Coulomb blockade effects in ultrafast tunnelling spectroscopy of the D_1 state, we kept the lightwave-driven current below one electron tunnelling per probe pulse at low probe-field strengths ($-0.07E_0$) (Extended Data Fig. 8d). In a regime of several electrons tunnelling per pulse, correlations and intrapulse effects may change the observed spectra. The sub-picosecond charge lifetime in the D_1 level, which is short compared with the pump–probe delay time ($\tau \geq 8.8$ ps),

ensures that a Coulomb blockade cannot cause the observed dynamical changes in the tunnelling spectra. Instead, horizontal shifts and vertical rescaling were attributed to shifts in energy levels and variations in the tip–sample distance, respectively. Coulomb blockade as well as other effects, such as energy levels that shift on occupation, challenge theory to realistically model LW-STs. Simplistic models like the instantaneous tunnelling model (Extended Data Fig. 2h and the subsequent paragraph) that do not take these effects into account are, therefore, not expected to reproduce the lightwave-driven spectra throughout the measured range.

Working in the regime of low peak fields also ensured that trailing the replica of the main THz pulse caused by reflections off a silicon beamsplitter did not pollute the data. A replica of the main pulse at around 21 ps after the main pulse reaches a peak amplitude of 37% of the main pulse and can alter the shape of the spectrum once the peak field of the main pulse reaches voltages higher than D_1 . In a simplistic model, the impact of the replica on the spectrum can be visualized by simulating the lightwave-driven current as an integral of the instantaneous tunnelling current based on the near-field waveform and steady-state dI/dV (Extended Data Fig. 2h). Additionally, fluctuations in the THz peak field might affect the exact shape of the peaks in LW-STs.

Extracting the energy onset of tunnelling into defect level D_1

To quantify the shift in tunnelling into the first defect level, we independently approximated the shape of the first tunnelling onset of $dI_{\text{LW}}^{\text{pr}}/dE_{\text{LW}}^{\text{peak}}$ (Fig. 4a,b) in all the curves by an error function (Extended Data Fig. 5a,b), fitting positive-value data up to a probe field of $0.1E_0$. We used the inflection point P of the error function as a measure of the tunnelling onset into the D_1 defect level. Hence, instead of assigning one specific point in the measured spectrum to D_1 , which is subject to noise, we consider several data points by fitting the tunnelling onset. All the data including error bars are fitted with three free parameters: position, amplitude and width. We extracted P as a function of the pump-field strength (Extended Data Fig. 5c) for $\tau = 10.2$ ps and $\tau = 8.8$ ps. Since vertical scaling is included in the fitting procedure, gap-size modulations do not contribute to the extracted level shift. Extended Data Fig. 5d shows the difference in energy-level shift between the two delay times as $P_{10.2\text{ps}} - P_{8.8\text{ps}}$. For the highest pump field ($0.320E_0$), the shift between $\tau = 10.2$ ps and $\tau = 8.8$ ps amounts to a field equivalent of $0.014E_0$ corresponding to a level displacement by approximately 40 mV. Considering the error bars, this shift is clearly visible in the lightwave-driven spectra.

Phonon band structure calculations of monolayer WSe_2 on Au(111)

We modelled a pristine WSe_2 monolayer on a Au(111) substrate by a $(\sqrt{3} \times \sqrt{3})R30^\circ$ superstructure⁵². Both substrate and tip were included as double layers of Au atoms (Au(111) slabs). We used a 4×4 supercell of the $(\sqrt{3} \times \sqrt{3})R30^\circ$ superstructure (in total 544 atoms). For calculating the total energies and forces on atoms, we employed density functional theory (DFT) with the Perdew–Burke–Ernzerhof exchange–correlation functional⁵³ and van der Waals interactions via DFT-D3 (ref. 54). Throughout the calculations, we used norm-conserving, dual-space pseudopotentials and a TZVP-MOLOPT Gaussian-type basis set to expand the Bloch states at the Γ point⁵⁵. All the DFT calculations were performed using the programme package CP2K (ref. 55). For geometry optimization, we kept all the Au atoms fixed, which stretches bonds in WSe_2 below 1% compared with the DFT-relaxed WSe_2 monolayer.

The phonon band structure (Fig. 5a) for fixed Au atom positions was calculated with the finite-displacement method implemented in the Phonopy package⁵⁶. We included a second WSe_2 layer (Extended Data Fig. 9) to compute the dispersion of the DM (Fig. 5a) under consideration of the internally enforced translational symmetry in the vertical direction. The convergence of the phonon band structure was

tested using four and six Au layers in the substrate slab instead of two layers. The shape of the DM band remains unchanged and its frequency at the Γ point increases by 28% and 30%. Other dispersion corrections (for example, the neglect of three-body terms in D3) yield a phonon frequency of DM at the Γ point within 10% discrepancy compared with the results from DFT-D3 (Fig. 5a).

The eigenvectors of DM at the Γ point extracted from the Phonopy calculation⁵⁶ exhibit a centre-of-mass motion of the TMDC layer, accompanied by an intralayer oscillation in the vertical direction (Fig. 5b; W atoms oscillate with an amplitude that is -150% of the amplitude of Se atoms).

Energy change in the D_1 defect level under DM oscillations

Assuming the same motion pattern for the defected WSe_2 monolayer as for the pristine WSe_2 monolayer, we discuss two mechanisms that cause a shift in the D_1 -defect-level energy on excitation of DM: the image charge effect⁴³ as a response to the shift in the whole layer and intracell distortion induced by DM (Fig. 5b).

In the experiment, two metal surfaces were close to the defect level—the metallic substrate and the metallic tip—motivating us to incorporate two image charges in our model (Fig. 5c (right), green dots). Assuming an infinitely localized unoccupied defect state, the image charge renormalization of the changes in the D_1 -defect energy level in response to an out-of-plane motion of Se atoms by Δz_{Se} as

$$\Delta E_{IC}(\Delta z_{Se}) = -\frac{e^2}{16\pi\epsilon_0} \left((z_1 - \Delta z_{Se})^{-1} - z_1^{-1} + (z_2 + \Delta z_{Se})^{-1} - z_2^{-1} \right),$$

where $z_1 = 2.1 \text{ \AA}$ and $z_2 = 5.5 \text{ \AA}$ describe the equilibrium distance of the defect to the image plane of the metal tip and metal substrate, respectively. Generally, the image charge effect is sensitive to the atomic geometry of the tip at such small distances. The image plane for an Au surface was assumed to be located 1.4 \AA outside of the outermost Au layer⁵⁷. Extrapolating the junction resistance to that of the point contact with its exponential distance dependence in the d.c. tunnelling regime, we extract a lower boundary of 3 \AA for the absolute distance between the tip and the upper Se layer. On this basis, we estimate the distance between the upper Se layer of WSe_2 and the tip in the contact mode to be 3.5 \AA , leading to $z_1 = 2.1 \text{ \AA}$. The value of $z_2 = 5.5 \text{ \AA}$ follows from the equilibrium distance of the WSe_2 monolayer to the Au substrate.

Intralayer displacements of W and Se atoms (Fig. 5b) slightly change the orbital hybridizations, and we quantified the effect on the D_1 -level energy using DFT calculations (Perdew–Burke–Ernzerhof functional) for a 12×12 supercell of monolayer WSe_2 with a single Se vacancy (in total 431 atoms; no Au atoms). We displaced Se (up to $\pm 10 \text{ pm}$) and W (-150% compared with Se) atoms according to the DM (Fig. 5c, right) for different DM amplitudes. The D_1 -level energy D_1^{PBE} (Δz_{Se}) was then extracted from the DFT calculations relative to the conduction band minimum $E_{CBM}^{PBE}(\Delta z_{Se})$ (Fig. 5c). To compare these results with the experiment, we assume that the measured oscillation amplitude (Fig. 4c, inset) corresponds to the oscillation amplitude of the top Se layer.

Data availability

The data that support the plots within this paper and other findings of this study are available from the publication server of the University of Regensburg at <https://doi.org/10.5283/epub.55247>. The input and output files for the calculation of the phonon band structure and defect-level energy shifts under DM displacement are available from the Novel Materials Discovery (NOMAD) repository at <https://doi.org/10.17172/NOMAD/2023.05.19-4>.

Code availability

All the DFT calculations have been done using the open-source package CP2K (development versions 10.0 and 2023.1). For the phonon band

structure calculations, we employed the Python package Phonopy (version 2.16.3).

References

- Velický, M. et al. Mechanism of gold-assisted exfoliation of centimeter-sized transition-metal dichalcogenide monolayers. *ACS Nano* **12**, 10463–10472 (2018).
- Bruix, A. et al. Single-layer MoS_2 on Au(111): band gap renormalization and substrate interaction. *Phys. Rev. B* **93**, 165422 (2016).
- Krane, N., Lotze, C., Läger, J. M., Reecht, G. & Franke, K. Electronic structure and luminescence of quasi-freestanding MoS_2 nanopatches on Au(111). *Nano Lett.* **16**, 5163–5168 (2016).
- Efron, B. *The Jackknife, the Bootstrap and Other Resampling Plans* (Society for Industrial and Applied Mathematics, 1982).
- Sarkar, S. & Kratzer, P. Signatures of the dichalcogenide–gold interaction in the vibrational spectra of MoS_2 and $MoSe_2$ on Au(111). *J. Phys. Chem. C* **125**, 26645–26651 (2021).
- Perdew, J. P., Burke, K. & Ernzerhof, M. Generalized gradient approximation made simple. *Phys. Rev. Lett.* **77**, 3865 (1996).
- Grimme, S., Antony, J., Ehrlich, S. & Krieg, H. A consistent and accurate ab initio parametrization of density functional dispersion correction (DFT-D) for the 94 elements H–Pu. *J. Chem. Phys.* **132**, 154104 (2010).
- Kühne, T. D. et al. CP2K: an electronic structure and molecular dynamics software package—Quickstep: efficient and accurate electronic structure calculations. *J. Chem. Phys.* **152**, 194103 (2020).
- Togo, A. & Tanaka, I. First principles phonon calculations in materials science. *Scr. Mater.* **108**, 1–5 (2015).
- Kharche, N. & Meunier, V. Width and crystal orientation dependent band gap renormalization in substrate-supported graphene nanoribbons. *J. Phys. Chem. Lett.* **7**, 1526–1533 (2016).
- Momma, K. & Izumi, F. VESTA 3 for three-dimensional visualization of crystal, volumetric and morphology data. *J. Appl. Cryst.* **44**, 1272–1276 (2011).

Acknowledgements

We thank I. Gronwald, M. Furthmeier and C. Rohrer for technical assistance and S. Refaely-Abramson, T. Preis, M. A. Huber, C. Echter, S. Maier, C. Meineke and M. Knorr for fruitful discussions. This work has been supported by the Deutsche Forschungsgemeinschaft (DFG, German Research Foundation) through Project-ID, 314695032 (C.R., L.Z.K., A.B., J.R., R.H. and Y.A.G.)—SFB 1277 (project B02) and through research grants RE2669/8 (J.R. and R.H.) and HU1598/9 (R.H. and J.R.), HU1598/7 (R.H.), HU1598/8 (R.H.) and Emmy Noether grant WI5664/3-1 (M.G. and J.W.). Funding from the ERC Synergy Grant MolDAM (no. 951519; J.R.) is gratefully acknowledged. We also gratefully acknowledge the computing time provided on the high-performance computers Noctua 2 at the NHR Center PC2. These are funded by the Federal Ministry of Education and Research and the state governments participating on the basis of the resolutions of the GWK for the national high-performance computing at universities (<https://www.nhr-verein.de/unsere-partner>).

Author contributions

J.R., R.H. and Y.A.G. conceived the project. C.R., L.Z.K., A.B. and Y.A.G. fabricated the samples, carried out the measurements and analysed the data together with J.R. and R.H. C.R., L.Z.K., A.B., J.R. and R.H. developed the rate equation model. M.G. and J.W. performed the ab initio calculations of the phonon spectrum and the vacancy's bound states. All authors contributed to the discussions of the results. C.R., J.R., R.H. and Y.A.G. wrote the manuscript with input from all authors.

Competing interests

The authors declare no competing interests.

Additional information

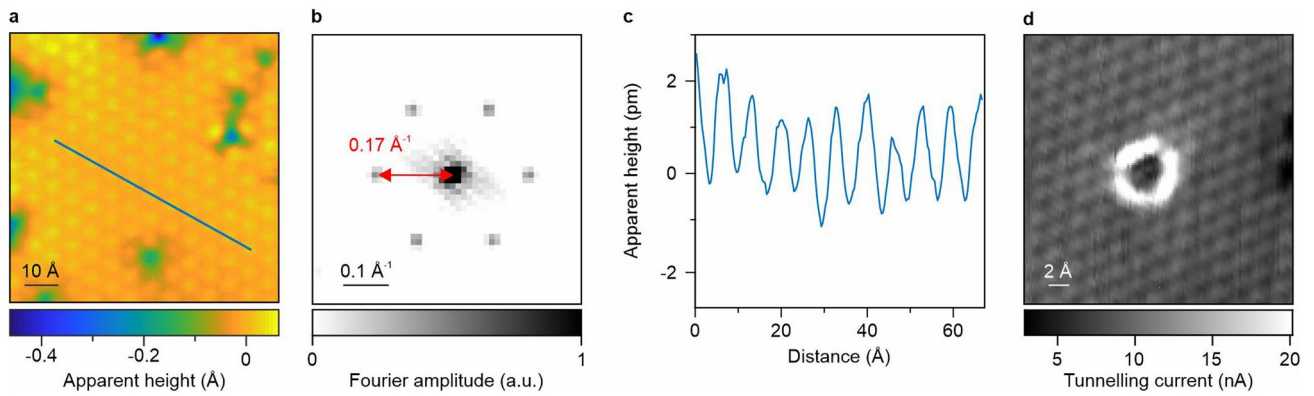
Extended data is available for this paper at <https://doi.org/10.1038/s41566-024-01390-6>.

Supplementary information The online version contains supplementary material available at <https://doi.org/10.1038/s41566-024-01390-6>.

Correspondence and requests for materials should be addressed to J. Wilhelm, J. Repp or R. Huber.

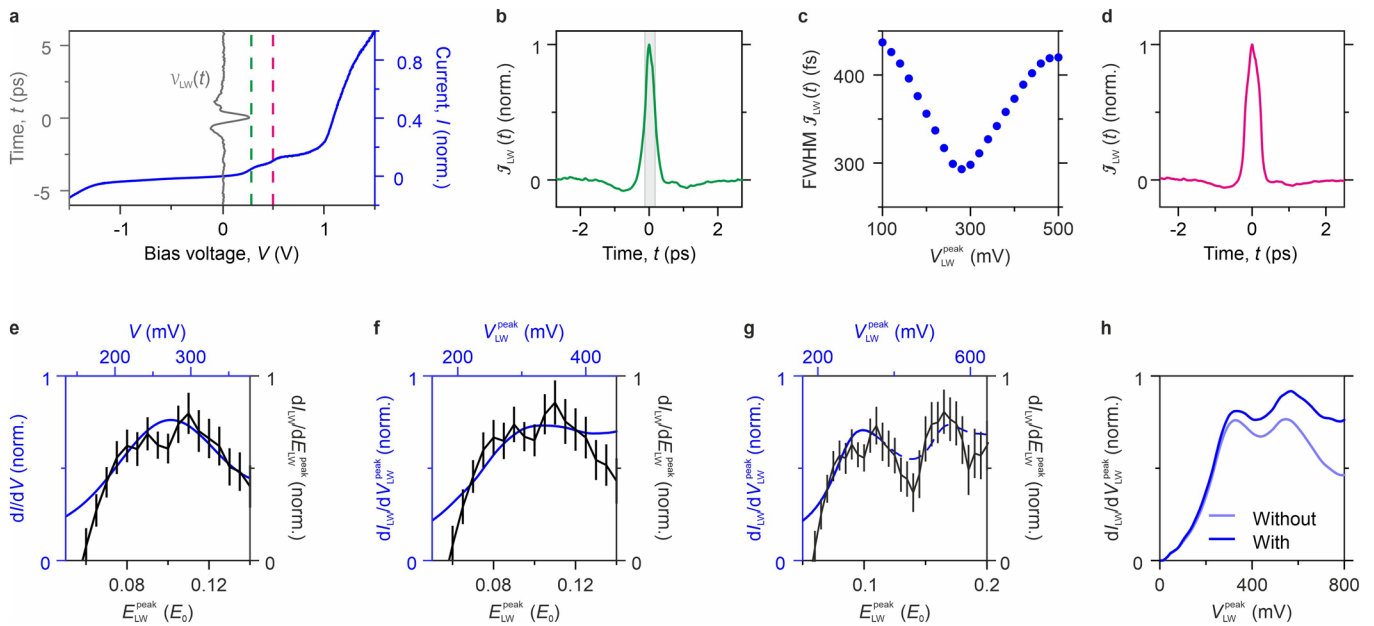
Peer review information *Nature Photonics* thanks Vedran Jelic, Zhen-Chao Dong, Katsumasa Yoshioka and Melanie Müller for their contribution to the peer review of this work.

Reprints and permissions information is available at www.nature.com/reprints.



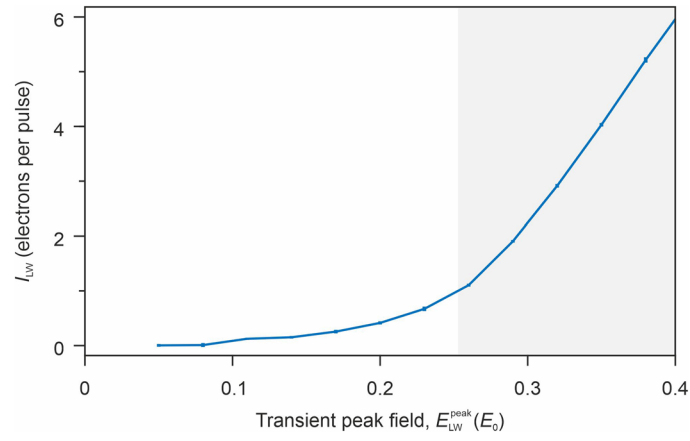
Extended Data Fig. 1 | Moiré pattern and atomic resolution of WSe₂ monolayer on Au(111). **a**, Constant-current STM image ($V = 1.12$ V, $I = 47.5$ pA). **b**, The Fourier transform of the STM image (**a**) yields a moiré period of ~ 6 Å.

c, The apparent height profile along the line marked in **a** exhibits a moiré-induced modulation of 2 picometres. **d**, Constant-height image of an atomic vacancy with atomic precision ($V = 600$ mV, height setpoint: $I = 49$ pA, $V = 359$ mV).



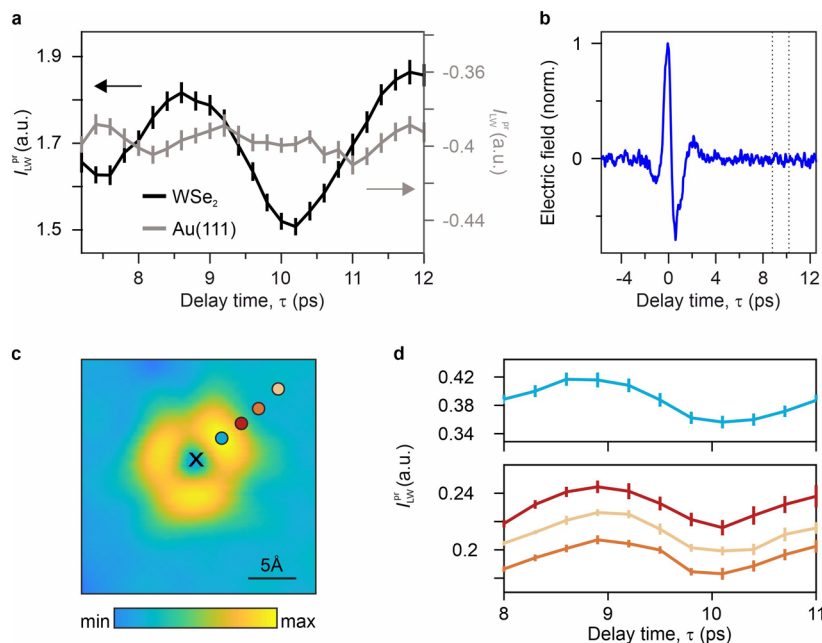
Extended Data Fig. 2 | Simulation of instantaneous current and lightwave-driven spectra. a, The near-field waveform measured with photon-assisted emission currents^{34,36} acts as transient bias voltage $V_{\text{LW}}(t)$ in the junction (grey curve). Time values correspond to the mutual delay between THz and optical pulse driving photon-assisted current. The blue curve shows the steady-state $I(V)$ curve measured on the orbital lobe. **b**, The instantaneous current $J_{\text{LW}}(t) = I(V_{\text{LW}}(t))$ determined by solving the rate equation with 5 fs lifetime in the limit of single-electron tunnelling per THz pulse is shown (green curve) for the near-field transient in **a** with its peak field tuned to the first defect level (280 mV, green dashed line in **a**). $J_{\text{LW}}(t)$ has a full width at half maximum (FWHM, grey area) of 296 fs, conventionally understood as the temporal resolution of LW-STM at a given peak field^{30,31}. **c**, The temporal resolution simulated with the rate equation model exhibits tunnelling windows of ~300 fs around D_1 . **d**, The

simulated instantaneous current for $V_{\text{LW}}^{\text{peak}} = 500$ mV (pink curve, dashed line in **a**), based on the rate equation model, rises steeply at the crest of the bias pulse owing to the additional tunnelling channel through D_2 . **e-g**, The peak field in the junction is calibrated by comparing the appearance of D_1 in the unpumped spectrum (data, black; data and error bars: see Fig. 1d, Se vacancy) with that in the steady-state spectrum (blue) (**e**), in the simulated spectrum based on the instantaneous tunnelling model (**f**) and the simulated spectrum based on the rate equation model (**g**). The calibration yields a peak field of 2.7 V, 3.2 V and 3.2 V, respectively, or (3.0 ± 0.3) V on average, consistent with photon-assisted measurements of the near-field waveform. **h**, The instantaneous tunnelling model without (light blue) and with taking reflections of the transient (dark blue) in the setup into account, exhibits an almost unchanged position of D_2 in the spectrum.



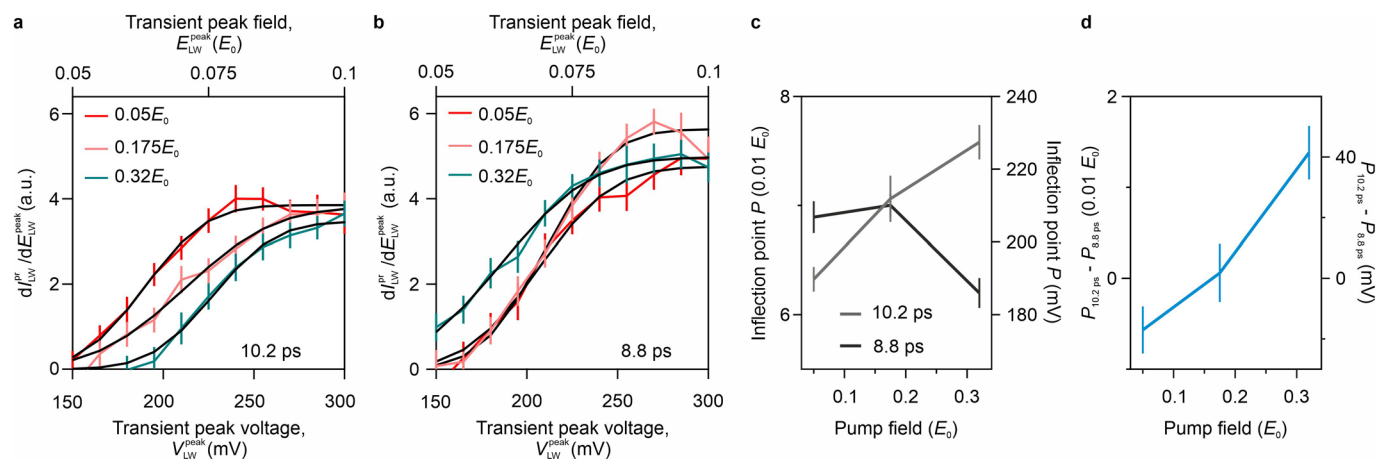
Extended Data Fig. 3 | Tunnelling onset on moiré peak. Lightwave-driven current I_{LW} measured on a moiré peak as a function of the peak field strength E_{LW}^{Peak} . The steep rise of the lightwave-driven current corresponds to tunnelling

into the conduction band at $-0.32E_0$. The regime of more than one tunnelling electron per pulse is highlighted in grey. Height setpoint: $V = 100$ mV, $I = 5$ pA, 2.9 Å approach.



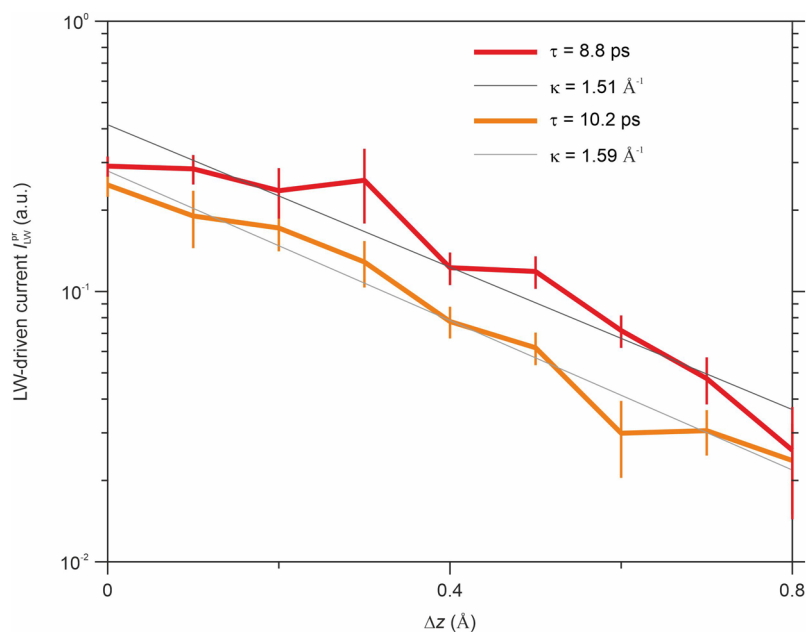
Extended Data Fig. 4 | Pump-induced oscillations of the tunnelling current for different tip positions. **a**, Black and grey curves show the lightwave-driven probe current ($0.6E_0$ peak field) as a function of delay time from the THz pump pulse ($0.33E_0$ peak field) on monolayer WSe_2/Au and bare $\text{Au}(111)$, respectively. The curves are recorded on different areas of the sample with the same tip. The comparison clearly demonstrates that the excitation mechanism is selective to the presence of WSe_2 (height setpoint for measurement on gold: $V = 30$ mV, $I = 5$ pA on $\text{Au}(111)$, 2.9 \AA approach). Note the almost constant current $I_{\text{LW}}^{\text{pr}}$ on bare Au, indicating that there are no trailing oscillations of the electric field of the pump pulse in this time window. This is further confirmed by photon-assisted measurements^{34,36} of the pump electric field in the junction (**b**). Delay times, at which spectra in Figs. 3,4 were measured are marked by dashed lines. **c**, Constant

current STM image showing the defect and four markers relative to the vacancy (cross) ($V = 380$ mV, $I = 49$ pA, colour bar: minimum to maximum apparent height). **d**, The lightwave-driven probe current ($0.3E_0$ peak field) as a function of delay time from the THz pump pulse ($0.175E_0$ peak field) shows the same phase and frequency for the four positions marked in **c**. The oscillations reveal only negligible deviations from harmonicity. Therefore, a potential drum-mode anharmonicity is unlikely to be responsible for the observed non-symmetric shifts of the D_1 tunnelling onset. Data in **a**, **d**: mean values \pm standard deviations of bootstrapped datasets (Methods). **a**: 32 (12) measurements per data point on Au (WSe_2), each measurement containing 18.3 million laser pulses. **d**: 9 measurements per data point, each: 109.8 million laser pulses.



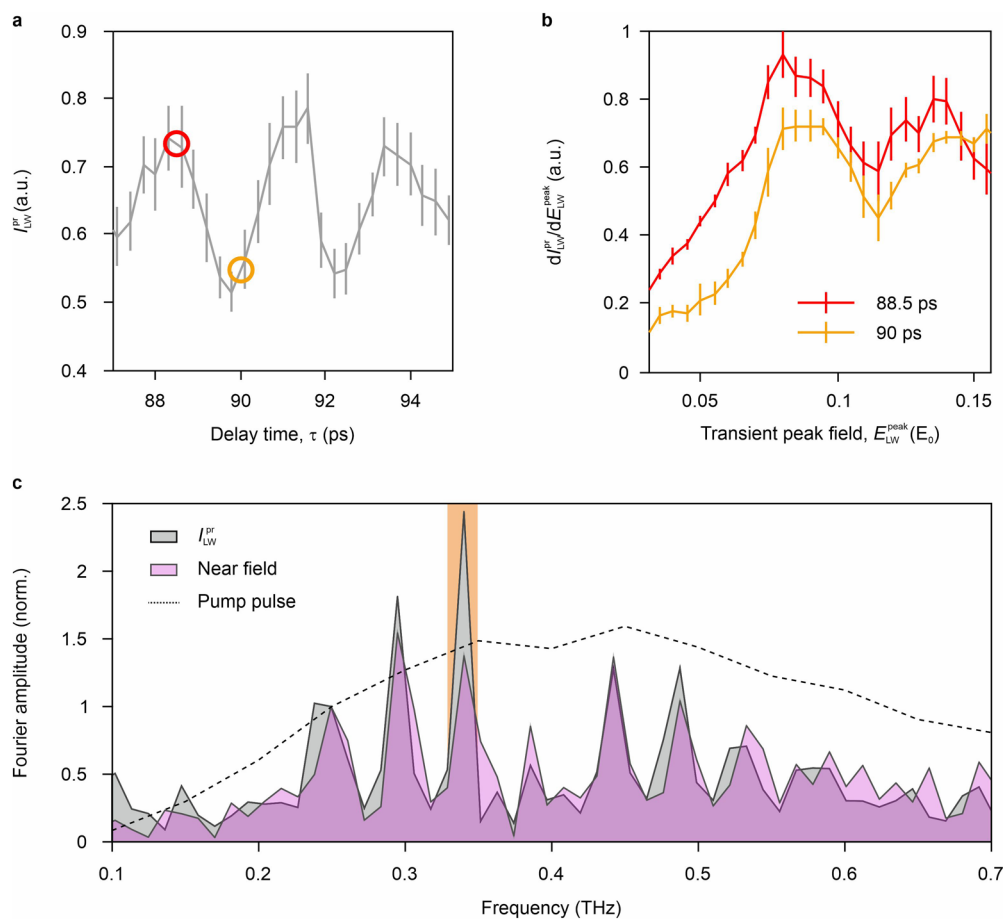
Extended Data Fig. 5 | Extraction of pump-field dependent shift of defect level D_1 . **a**, Ultrafast tunnelling spectra (data, coloured) for three different pump peak voltages at a pump-probe delay $\tau = 10.2$ ps are fitted with error functions (black curves). Statistics and error bars: see Fig. 3c and Fig. 4a,b. **b**, Equivalent data and fits for a pump-probe delay time of $\tau = 8.8$ ps. **c**, Data points: inflection point P of the respective error function fit as a function of the pump peak field

for delay times $\tau = 10.2$ ps and $\tau = 8.8$ ps used as a measure of the tunnelling onset into the first defect level. **d**, Difference of the inflection points at $\tau = 8.8$ ps and 10.2 ps (**c**) as a measure of the ultrafast energy shift of the tunnelling onset. The error bars in **c** and **d** are one standard deviation on the parameter fit of the inflection point.



Extended Data Fig. 6 | Lightwave-driven current as a function of tip-sample distance. Red and orange curves show the exponential scaling of the lightwave-driven current $I_{LW}^{pr} \propto \exp(-2\kappa\Delta z)$ with change in tip-sample distance Δz for both delay times, $\tau = 8.8$ ps and $\tau = 10.2$ ps, between pump ($0.32 E_0$ peak field) and probe ($0.3 E_0$ peak field) pulses. Linear fits to the logarithm of $I_{LW}^{pr}(\Delta z)$ (grey

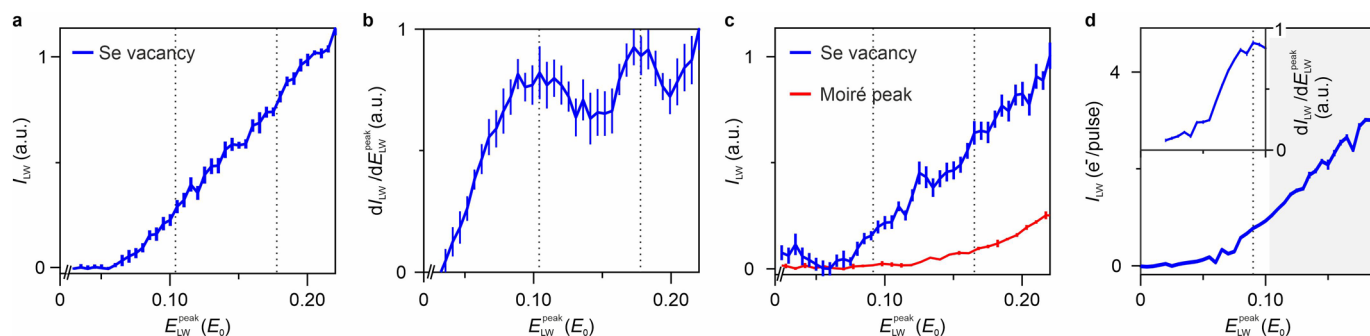
curves) yield the decay constants $\kappa = 1.5/\text{\AA}$ and $1.6/\text{\AA}$, respectively. The mean decay constant amounts to $\kappa = 1.55/\text{\AA}$. $\Delta z = 0$ corresponds to the height setpoint of $V = 30$ mV, $I = 49$ pA, 1.8\AA approach. Each data point: mean value \pm standard deviation of 8 bootstrapped measurements (Methods). Each measurement covers a span of 109.8 million laser pulses.



Extended Data Fig. 7 | Long-lived dynamics of the atomic defect.

a, Oscillations of the lightwave-driven tunnelling current induced by THz excitation can be seen up to 100 ps after excitation on an orbital lobe of the vacancy in monolayer WSe₂/Au(111). Pump and probe peak fields, $0.32 E_0$. **b**, LW-STs for delay times $\tau = 88.5$ ps (red) and 90 ps (yellow) exhibit the same phase dependence as for $\tau = 8.8$ ps and 10.2 ps (Fig. 3c): at a minimum of the current oscillations (yellow circle in **a**), the tunnelling onset into D₁ is shifted to higher energies. Pump peak field, $0.46 E_0$. **c**, Fourier transforms of pump-probe traces of the lightwave-driven current for $7 \text{ ps} < \tau < 95 \text{ ps}$ (grey) and corresponding delay-time interval of the near-field waveform of the pump

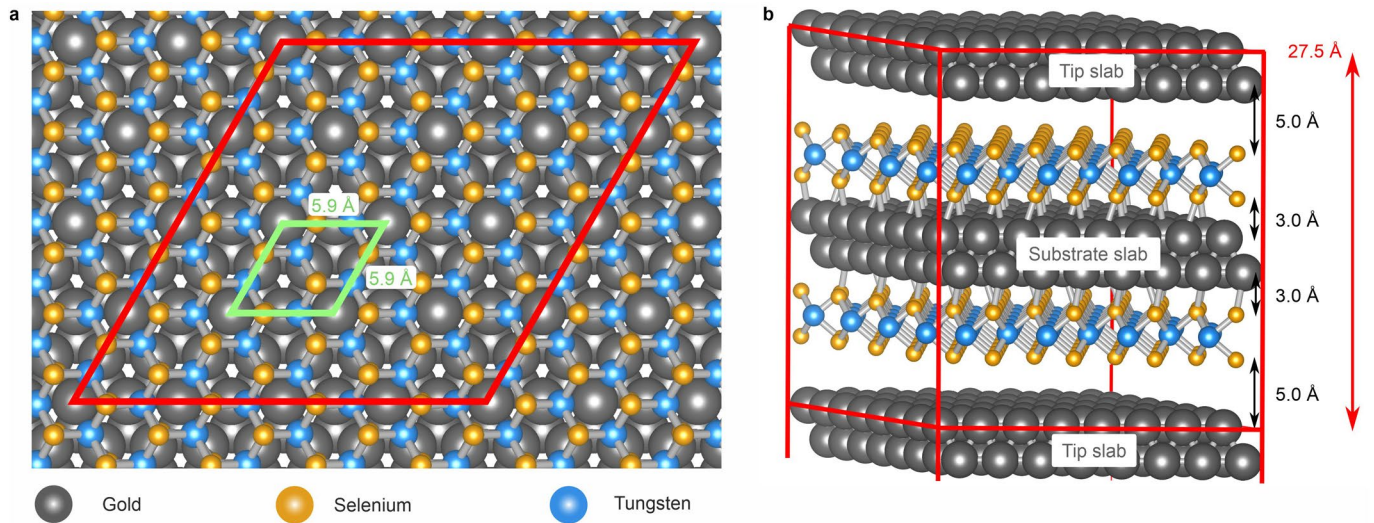
pulse containing its time-delayed replicas (Methods) (pink). The latter result in a multi-peak spectrum present in both traces featuring an envelope similar to the pump pulse itself (dashed). A pump-probe current trace reveals the strongly enhanced peak at 0.34 THz (orange shaded area), which we can attribute to the drum mode frequency. The Fourier amplitudes are normalised to their values at 0.25 THz. Data in **a**: mean values \pm standard deviations of bootstrapped datasets (Methods); 12 measurements per data point, each measurement: 18.3 million laser pulses. **b**: mean value \pm standard deviation of 2 datasets, each measurement: 219.6 million laser pulses.



Extended Data Fig. 8 | I_{LW} and its derivative for different Se vacancies.

a, Raw data of I_{LW} on a different Se vacancy than the one investigated in Fig. 1 demonstrates that the LW-STs procedure is robust (height setpoint: $V = 100$ mV, $I = 4.9$ pA, 2.9 Å approach). **b**, The derivative of smoothed I_{LW} shown in **a** yields two defect levels. **c**, Non-smoothed data of tunnelling current shown in Fig. 1c. **d**, I_{LW} without artefactual reflection sources (see Methods) and its derivative (inset)

showing the tunnelling onset into D_1 . The current I_{LW} approaches zero for low peak fields $E_{\text{LW}}^{\text{peak}}$. The regime of more than one tunnelling electron per pulse is highlighted in grey. Data in **a-c**: mean values \pm standard deviations of bootstrapped datasets (Methods), each measurement containing 219.6 million laser pulses. **a,b**: 5 measurements per data point. **c**: 5 (2) measurements per data point on Se vacancy (Moiré peak).



Extended Data Fig. 9 | Ball-and-stick representation of the atomic geometry for calculating the phonon band structure of WSe₂ on Au(111). We employ a 4×4 supercell of the $(\sqrt{3} \times \sqrt{3})R30^\circ$ structure, cell boundary is marked with red lines. **a**, Top view. The moiré lattice period of 5.9 Å results from the lattice

constant of 4.17 Å of bulk Au. **b**, Side view with Au(111) surface slab representing the tip, Au(111) substrate slab and two WSe₂ monolayers (in total 544 atoms). Visualisation of the atomic geometry was done using Vesta⁵⁸.